fluids

Article

Experimental Investigation of Anisotropic Invariants in Streams with Rigid Vegetation and 3D Bedforms

Kourosh Nosrati [1], Ali Rahm Rahimpour [1], Hossein Afzalimehr [1], Mohammad Nazari-Sharabian [2,*] and Moses Karakouzian [3]

[1] Natural Disasters Prevention Research Center, School of Civil Engineering, Iran University of Science and Technology, Tehran 16846-13114, Iran
[2] Department of Mathematics, Engineering and Computer Science, West Virginia State University, Institute, WV 25112, USA
[3] Department of Civil and Environmental Engineering and Construction, University of Nevada Las Vegas, Las Vegas, NV 89154, USA; mkar@unlv.nevada.edu
* Correspondence: m.nazari@wvstateu.edu

Abstract: The presence of vegetation in submerged conditions and bedforms are a reality in coarse-bed streams. However, this reality has not been well investigated in the literature, despite being a major challenge for natural stream restoration. In order to control many unknown factors affecting prototype scale, this experimental study has been conducted in a laboratory flume, considering 3D bedforms. The results of this study show that 3D bedforms with submerged vegetation elements may change all estimations from 3D to 2D forms near the bed due to the change in roughness. This will change the classic determinations of resistance to flow and sediment transport via Reynolds stress and turbulent flow and may lead to more-affordable complex hydraulic process modeling.

Keywords: 3D bedforms; laboratory experiments; submerged vegetation; Reynolds stress; turbulent flow

check for updates

Citation: Nosrati, K.; Rahm Rahimpour, A.; Afzalimehr, H.; Nazari-Sharabian, M.; Karakouzian, M. Experimental Investigation of Anisotropic Invariants in Streams with Rigid Vegetation and 3D Bedforms. *Fluids* **2024**, *9*, 282. https://doi.org/10.3390/fluids9120282

Academic Editors: Jaan H. Pu and Chandrashekhar S. Jog

Received: 17 October 2024
Revised: 26 November 2024
Accepted: 26 November 2024
Published: 28 November 2024

1. Introduction

River researchers have extensively examined the flow dynamics through submerged rigid vegetation using a combination of experimental and numerical approaches to assess the effects of vegetation on flow structure and its implications for hydraulic resistance, mixing processes, turbulent structures, and sediment transport [1–19]. One commonly examined aspect in fluid dynamics studies is the anisotropic nature of turbulence, which refers to how much it deviates from isotropic turbulence. Isotropic turbulence occurs when velocity fluctuations remain consistent regardless of axis rotation [20]. Therefore, the Reynolds normal stresses (σ_x, σ_y, and σ_z, representing the streamwise, spanwise, and vertical directions, respectively) can be seen as constant. Conversely, turbulence displays anisotropy when the Reynolds normal stresses change with the direction, indicating that temporal velocity fluctuations exhibit a preferred orientation compared to others. The Reynolds stress anisotropy tensor is a useful method of assessing anisotropy in turbulent flows, employing the anisotropic invariant map (AIM) known as the Lumley triangle. First proposed by Lumley and Newman (1977) [15], this approach represents a two-dimensional space defined by the invariant characteristics of the Reynolds stress anisotropy tensor b_{ij}:

$$b_{ij} = \frac{\overline{u_i' u_j'}}{2k} - \frac{1}{3}\delta_{ij} = \frac{\overline{u_i' u_j'}}{\overline{u_i' u_i'}} - \frac{1}{3}\delta_{ij}. \quad (1)$$

At the vertex representing velocity fluctuation, the average of the square of velocity fluctuations ($\overline{u_i' u_i'}$) is related to twice the turbulent kinetic energy ($k = 0.5\,\overline{u_i' u_i'}$), utilizing the Einstein notation, while δ_{ij} denotes the Kronecker delta function (equal to 1 if i = j, and

0 otherwise). In general, for anisotropic flows (like those in boundary layers or wakes), the tensor can vary more widely, but the trace of the tensor is typically constrained to obey the following: $b_{xx} + b_{yy} + b_{zz} = 0$

In practice, this means that the values of b_{ij} are constrained by physical conditions, and numerical studies have shown values that can span from near-zero (in quasi-2D flows) to values approaching the upper limits in turbulent conditions, where the flow becomes inviscid or highly anisotropic [21,22]. The precise numerical range of b_{ij} would depend on the specific turbulence models or experimental flow settings being considered. In summary, while the components may vary, they generally follow constraints derived from turbulence theory and modeling. The variation range of the Reynolds stress anisotropy tensor b_{ij} can significantly differ depending on the location within a fluid flow, particularly in open channel flows, where conditions near the boundary (e.g., the bed) and the free surface can lead to distinct flow characteristics. Near the bed, turbulence is influenced heavily by the frictional interaction with the surface. The flow is typically characterized by high shear stresses. In this region, the anisotropy is often dominated by the streamwise and wall-normal components, leading to significant values of b_{11} (streamwise) being larger than b_{22} (vertical) and b_{33} (spanwise). Values of b_{ij} can have the following ranges [23]:

- b_{11} being positive, approximately 0.5 to 1;
- b_{22} often being negative, around -0.5 to -1;
- b_{33} usually being the smallest magnitude, tending toward a negative value but less than b_{22}.

The region near the water surface often experiences reduced turbulence intensity and a different flow organization. Turbulence here can be less organized due to the damping effects of the surface, leading to different interactions. The spanwise component can become more significant due to the influence of surface waves or atmospheric effects. Values of b_{ij} may range as follows [23]:

- b_{11} can still be higher but typically lower than near the bed, possibly ranging around 0.2 to 0.5;
- b_{22} may shift towards less negative values or become zero, i.e., ranging from 0 to -0.5;
- b_{33} may be less negative or even positive under certain conditions representing surface fluctuations.

In summary, the anisotropy tensor b_{ij} near the bed exhibits higher values and distinct shear-dominated patterns, while near the water surface, the values tend to be less pronounced and reflect more isotropic conditions. The precise values will depend on specific flow characteristics, turbulent intensity, and experimental or simulation setups. The magnitude of anisotropy generally decreases from the bed toward the surface, as the influence of wall effects diminishes and the flow becomes less influenced by shear. The specific ranges can vary significantly depending on the flow conditions (e.g., depth, velocity, turbulence intensity) and the characteristics of the fluid (e.g., density, viscosity) [23].

Consequently, the AIM is visualized as a triangle on a (I_3, $-I_2$) plane, with I_2 denoting the level of anisotropy and I_3 representing the type of anisotropy (Figure 1). The boundaries of this triangle are indicative of the turbulent state (1D, 2D, or 3D turbulence) and processes (axisymmetric expansion, axisymmetric contraction, and two-component turbulence). Specifically, I_2 and I_3 stand for the second and third invariants of the Reynolds stress anisotropy tensor, respectively, and can be mathematically expressed as described in the reference by Dey et al. (2020) [11].

$$I_2 = -\frac{b_{ij}b_{ij}}{2} = -\left(\lambda_1^2 + \lambda_1\lambda_2 + \lambda_2^2\right), \tag{2}$$

$$I_3 = \frac{b_{ij}b_{jk}b_{ki}}{3} = -\lambda_1\lambda_2(\lambda_1 + \lambda_2), \tag{3}$$

where λ_1 and λ_2 are the anisotropy eigenvalues.

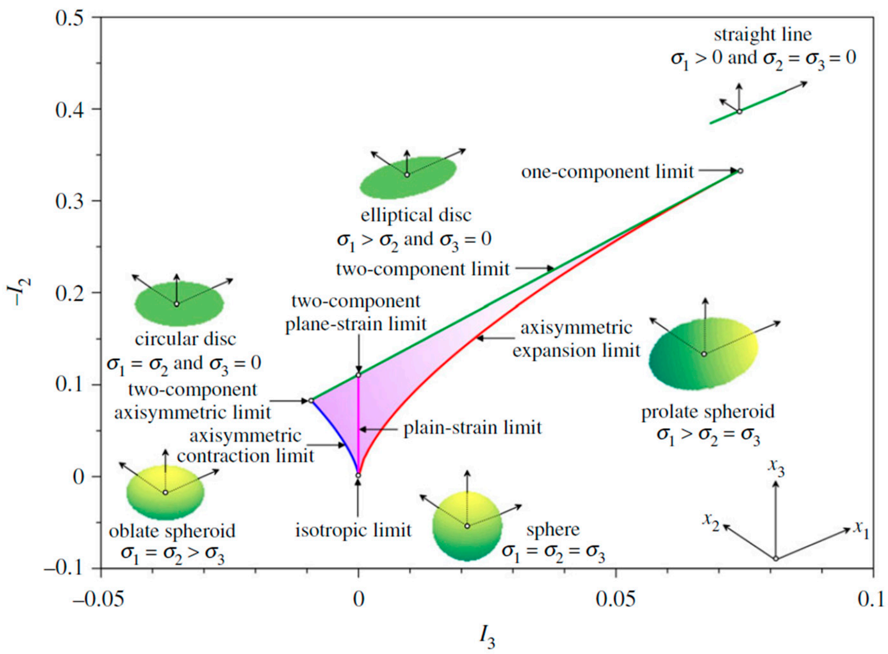

Figure 1. A visual representation of the anisotropy invariant map concept.

The AIM's left curve can be characterized by the equation $I_3 = -2\left(-I_2/3\right)^{3/2}$, indicating a scenario in which two diagonal components of the Reynolds stress tensor surpass the third, resulting in a pancake-shaped turbulence. Consequently, the stress ellipsoid takes the form of an oblate spheroid, where $\sigma_x = \sigma_y > \sigma_z$. The left extremity of the curve signifies the two-component axisymmetric limit, leading to a circular disk-shaped stress ellipsoid $(\sigma_x = \sigma_y$, and $\sigma_z = 0)$. Conversely, the right curve denotes a situation where one component of the Reynolds stress tensor dominates the other two, causing a cigar-shaped turbulence and a prolate spheroid stress ellipsoid $(\sigma_x = \sigma_y < \sigma_z)$. The right end of the curve represents the one component limit, resulting in a linear stress ellipsoid $(\sigma_x > 0$ and $\sigma_y = \sigma_z = 0$, or $\sigma_z > 0$ and $\sigma_x = \sigma_y = 0)$. The equation $I_3 = 2\left(-I_2/3\right)^{3/2}$ defines the right curve of the AIM. The upper boundary of the AIM corresponds to 2D turbulence, characterized by an elliptical disk-shaped stress ellipsoid $(\sigma_x > \sigma_y$, and $\sigma_z = 0)$, which is expressed as $I_3 = -(9I_2 + 1)/27$. Finally, the lower cusp of the AIM pertains to 3D isotropic turbulence, where the stress ellipsoid takes the form of a sphere $(\sigma_x = \sigma_y = \sigma_z)$. Turbulence anisotropy is a prevalent characteristic in intricate fluid dynamics, as seen in environments like vegetated channels [24]. Caroppi et al. (2018) utilizes anisotropy invariant maps (AIMs) to examine how submerged rigid cylinder vegetation influences turbulent structures in flow over a smooth bed [25]. Their analysis shows two-component isotropic turbulence in the viscous sublayer near the bed, which transitions to a quasi-one-dimensional state as one moves towards the canopy top. Beyond the canopy, turbulence exhibited an axisymmetric expansion, trending towards a two-dimensional isotropic state. Penna et al. (2020) has explored the anisotropy of turbulent flows in the presence of aligned cylinder arrays mimicking rigid vegetation on rough beds [26]. They have noted a shift from axisymmetric anisotropy to quasi-three-dimensional isotropy near the water surface due to the combined effects of vegetation and bed roughness, particularly noticeable with the finest sediment diameter used in their experiments. Barman and Kumar (2022) have investigated turbulence anisotropy in a compound channel featuring a mix of submerged and emergent vegetation [10]. Their findings indicate that a channel section with 67% emergent vegetation displays a stronger inclination towards two-dimensional turbulence compared to other non-uniform vegetation configurations. Given that the Reynolds stress anisotropy largely signifies the presence of organized motion and plays a significant role in momentum transport [27], studying it is vital to comprehend and model turbulence [25] and sediment transport processes in vegetated flows [28]. Hence, this study aims to describe turbulence anisotropy using AIMs in turbulent flows passing through random and emergent rigid vegetation on rough beds, emphasizing the impact of both roughness and vegetation distribution. Kumar et al. (2023) have conducted experimental research on flow turbulence and Reynolds stress anisotropy in flow over a smooth rigid bed with emergent rigid vegetation in a straight channel [29]. The results show that the anisotropy tensor's longitudinal distribution near the bed surface in the vegetation zone creates higher anisotropic flow than in the non-vegetation zone, where the transverse and vertical distributions of the tensor are associated with lower anisotropic flow.

The reviewed literature offers a detailed analysis of turbulence anisotropy in flow scenarios affected by submerged rigid vegetation and rough beds, providing valuable insights into the intricate dynamics of turbulence structures in vegetated and compound channels with different vegetation types. Although existing literature extensively explores the effects of vegetation and bed roughness on turbulence properties, a critical evaluation reveals a significant gap in the research on Reynolds stress anisotropy, particularly in flows over 3D pools with submerged rigid vegetation. Despite in-depth investigations into turbulence anisotropy patterns and behaviors concerning vegetation layouts and bed roughness, current studies appear to lack attention to 3D pools. Understanding Reynolds stress anisotropy in flows over 3D pools with submerged rigid vegetation is essential to unravel the organized movements and momentum transfer in such environments. By focusing on this specific scenario and delving into the intricacies of turbulence anisotropy within 3D pools, researchers may unveil distinctive insights into the interactions and influence of these features on flow dynamics. Hence, there is a clear imperative for future research to address this research gap through comprehensive studies that detail Reynolds stress anisotropy in flows over 3D pools with submerged rigid vegetation. By addressing this gap, researchers can enhance our understanding of turbulence in complex flows and improve models for predicting flow behaviors in natural and engineered systems.

2. Materials and Methods

The Materials Laboratory experiments were conducted in a flume that was 0.9 m wide, 14 m long, and 0.6 m deep in the Iran University of Science and Technology (as shown in Figure 2). The entrance depth to the studied classic bedform of coarse-bed rivers, which is in a pool shape (H) upstream of the uniform flow, was set at 44 cm, and was consistent throughout each Run, adjustable by a vertical gate at the end of the flume, chosen based on field observations [30]. The flow rate (Q) was maintained at a constant value of 31.7 ± 0.1 L per second using a flow meter. The PROMAG 10w magnetic water flowmeter, capable of measuring velocity flow from 0.01 up to 10 m/s and operating at temperatures up to 80 degrees, is utilized in this research. The Reynolds numbers and Froude numbers indicated fully turbulent flow ($Re > 2000$) and sub-critical flow conditions ($Fr < 1$) in all tests [31].

Bedforms in rivers typically develop as interconnected 3D sequences of pools and riffles rather than isolated features. Accurately replicating these natural formations in a laboratory setting presents significant challenges, especially in coarse-bed rivers, where bedforms are highly complex and irregular across different reaches. This complexity poses a notable limitation in fluvial engineering and restoration projects. Nonetheless, advancing knowledge in river restoration requires engineers and researchers to use simplified laboratory models to identify patterns that align with natural river systems.

To support this effort, a total station camera was utilized to capture the 3D profiles of bedforms (pools and riffles) along a 200-m river reach. The survey employed a 30×30 cm grid across 20 cross-sections. The collected topographic data were processed in a GIS package to create a digital elevation model (DEM), allowing for detailed analysis of the 3D bedform structures. Field investigations focused on determining the general slopes of pool entry and exit sections in a gravel-bed river, alongside the grain size of the bed material and prevailing flow conditions.

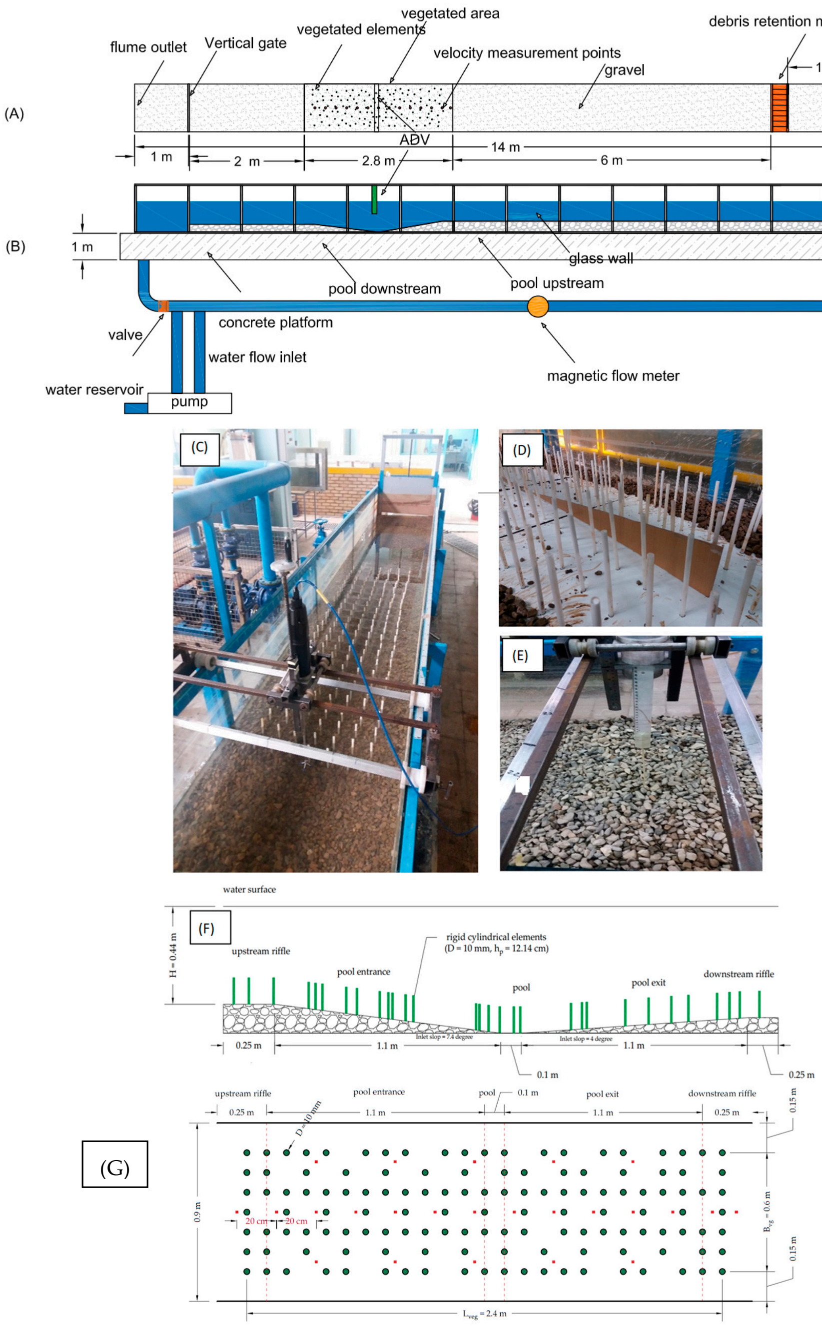

Figure 2. (**A**) Experimental setup; (**B**) plan view; (**C**) side view; (**D**) the bed topography was mapped using a ruler attached to an ADV device; (**E**) a wooden template shaped like a right-angled triangle; (**F**) vegetation was simulated with plastic pipes; (**G**) longitudinal section of the pool. The red square dots indicate the sampling positions for flow velocity (e.g., Run I).

Using these data, a laboratory flume was constructed to replicate the dominant bedforms of the Kheirabad River in southern Iran. The flume pool closely mirrored the river's morphology, grain size, and flow depth. The pool–riffle morphology observed in the reach under study served as a representative model for understanding dominant bedform characteristics in gravel-bed rivers.

The bedform was placed at least 6 m from the channel's start to ensure turbulent boundary layer development and uniform upstream flow. Additionally, to ensure complete turbulent boundary layer development, velocity profiles were obtained at intervals of 400 to 600 cm from the channel start, with a step of 50 cm (Figure 2A). The bedforms were placed 6 m from the channel start to avoid interference from the vertical gate at the flume;s end, with the gate's impact estimated to extend approximately 1.6 m [6,30]. Consequently, the pools were positioned around 2 m from the channel's end to prevent this interference (Figure 2A,B). The slopes of the pool were determined using a wooden template shaped like a right-angled triangle, where the angle at the base determined the slope of the pool (Figure 2D). The bed topography was mapped using a ruler attached to an ADV device for vertical movement (Figure 2E). Vegetation was simulated with plastic pipes placed on a wooden base at varying densities (Figure 2D). The vegetation elements were rigid, submerged, and spaced uniformly on the bed surface (Figure 2C). In the primary experimental phase (Run I), 44 elements were selectively removed to introduce a disordered and stochastic distribution of vegetated elements within the pool. Subsequently, each Run of experiments employed 131 elements for the initial density, 87 for the intermediate density, and 43 for the final density (Runs II and III). Additionally, to facilitate result comparisons, all experiments were conducted in a vegetation-free bed (bare channel in Run IV). To simulate submerged vegetation, many rigid plastic cylindrical elements with a diameter (D) and mean height $\left(\bar{h}_{\mathrm{p}}\right)$ of 10 mm and 12.14 cm, respectively, were placed in a bed with an irregular array (Figure 2F). Table 1 summarizes the experimental conditions, where u represents the average flow velocity, u_{c} is the maximum velocity, u^{*} is the shear velocity, $Re = uH/\vartheta_m$ is the Reynolds number, and $Fr = u/(gD_h)^{0.5}$ is the Froude number at the pool's inlet. The shear velocity u^{*} was determined using turbulence kinetic energy ($u^{*}{}_{TKE}$). In this method, bed shear stress is estimated as $\tau_{TKE} = 0.5c_2\rho\left[\overline{u'^2} + \overline{v'^2} + \overline{w'^2}\right]$, from which shear velocity is calculated using $u^{*}{}_{TKE} = (\tau_{TKE}/\rho)^{0.5}$. Here, c_2 is a constant valued at 0.19, ρ is 9810 kg/m^3, u', v', and w' are the velocity components, which are longitudinal, transverse, and perpendicular to the flow, with D_h representing the hydraulic depth and ϑ_m indicating the kinematic viscosity of water at 25 degrees Celsius.

Table 1. Experimental conditions.

Runs	Vegetation Density ∅	d_{50} (mm)	H(m)	Q (L/s)	Bedform Amplitude Δ	Ratio Δ/λ	u/uc	u/u^*	$\bar{h}_{\mathrm{p}}/H$	Re	Fr
Run I	0.007	23.3	0.44	31.7	0.1428	0.051	0.80	0.14	3.55	54,084.71	0.06
Run II	0.0047	23.3	0.44	31.7	0.1428	0.051	0.80	0.12	3.55	50,155.83	0.05
Run III	0.0023	23.3	0.44	31.7	0.1428	0.051	0.80	0.13	3.55	40,124.67	0.04
Run VI	0	23.3	0.44	31.7	0.1428	0.051	0.80	0.17	3.55	55,902.15	0.06

As shown in Table 1, three area densities of vegetation were used, namely, $\varnothing = 2.3 \times 10^{-3}$, 4.7×10^{-3}, and 7×10^{-3}, where $\varnothing = A_{\mathrm{r}}\pi D^2/4$ is defined as the area density of vegetation, $A_{\mathrm{r}} = N/\left(L_{\mathrm{veg}} \times B_{\mathrm{veg}}\right), N$ is the total number of vegetation elements [5,32], and $L_{\mathrm{veg}} = 2.4$ m and $B_{\mathrm{veg}} = 0.6$ m are the length and width of the vegetated area along with the streamwise and spanwise directions, respectively. It is important to highlight that the vegetated elements at all densities are rigid and fully submerged, lacking flexibility. Since the flow depth differs from the initial section of the bedform to its terminus, the relative submergence (the ratio of the flow depth to the average height of the vegetated element) will vary across the various experiment series [33]. Nevertheless, the relative submergence in this study ranges from 2.1 to 4.6. The measurements were carried out in a vegetation-free pool to contrast the findings with those obtained in a pool with vegetation. A man-made pool was built in the laboratory within a linear channel, following the methodology outlined by Nosrati et al. (2024), as detailed in Table 1. However, the entrance and exit slopes were 7.4 and 4 degrees, respectively [7,30]. The pool–riffle amplitude (Δ) was determined by the residual pool depth [34,35], which was defined as the difference in elevation between the riffle crest and the pool bottom (Table 1). With a constant bedform wavelength $(\lambda = 2.8$ m), the ratio of the pool amplitude to the wavelength, Δ/λ, had a value of 0.051 in this study. As shown in Figure 3, the gravel particle size of bed material used in the experiments ranged from 5 to 50 mm, with a median grain size of $d_{50} = 23.3$ mm , $d_{16} = 14$ mm, and $d_{84} = 40$ mm. In reality, the choice of materials for bed grading has involved selecting four gradings from the beginning, middle, and end of the river's gravel bed based on Wolman's method (1954), using data from previous studies [5–7,30]. Subsequently, materials for the laboratory channel bed were chosen based on approximations made within these classifications. Previous research indicates that bed particle diameters in pools can range from 4 to 75 mm [7,30,36,37]. To determine the critical velocity (u_c) necessary to assess bed particle movement in the channel, the formula $u_c = (2.5(H/d_{50})^{0.2} g(\rho_s/\rho - 1)d_{50})^{0.5}$ was employed [38]. In all experiments, the flow velocity was kept below u_c, indicating the stability of bed particles. Notably, the objective of these studies did not involve sediment transport analysis.

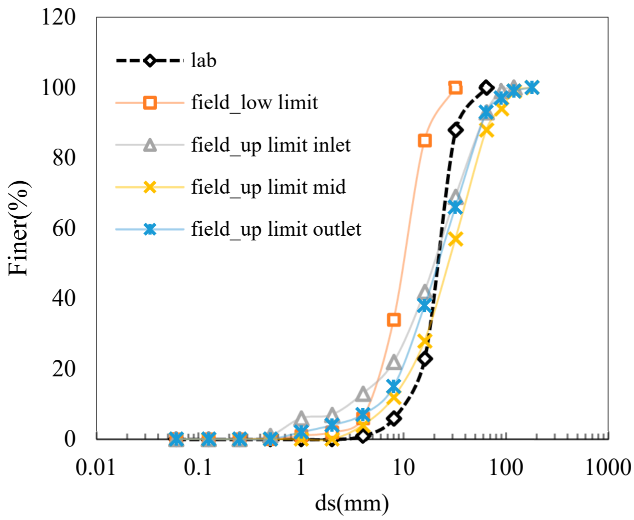

Figure 3. Particle size distribution curve of bed sediment.

A down-looking acoustic Doppler velocimeter (ADV) developed by Nortek was used to measure the instantaneous three-dimensional velocity components. The first point of measurement was set at a distance of 4 mm from the bed. The WinADV package for data processing prepared by Nortek was used to filter and process velocity and turbulence data [39,40]. However, data with an average correlation coefficient of less than 70% and an average SNR of less than 15 dB were filtered out [39,40]. Each velocity profile was developed based on the mean velocity measured at 23 to 33 points from the point located at 4 mm above the vegetated elements (12.56 cm from bed) to the point located at 5 cm below the water surface. In addition, velocity measurements were made at 14 cross-sections along the riffle–pool–riffle channel from the cross-section 20 cm upstream to the cross-section 20 cm downstream of this channel (Figure 2G) [5,6,30]. Due to so many measured velocity data, all analyses were performed in control sections for each Run at the upstream section of the pool $(X/\lambda = 0.017)$, the pool entrance $(X/\lambda = 0.21)$, the middle of the pool $(X/\lambda = 0.5)$, the pool exit $(X/\lambda = 0.78)$, and the downstream section of the pool $(X/\lambda = 0.98)$, where X is the longitudinal distance. All computations concerning anisotropy-invariant maps were carried out through Python ver. 3.12.0 programming.

3. Results

This section studied the evolution and variations of anisotropic turbulence in the flow direction within a 3D pool, focusing on the central region of a channel with irregularly distributed vegetated elements at varying densities, as well as in a bare channel. These locations included the uniform flow section upstream of the pool (X/"λ" = 0.017), the decelerating flow section (X/"λ" = 0.21), the middle of the pool (X/"λ" = 0.5), the accelerating flow section (X/"λ" = 0.78), and the downstream section of the pool under study

(X/"λ" = 0.98). This study utilized anisotropy-invariant maps derived from the stress tensor with the findings presented in Figures 4–7. Specifically, the anisotropy-invariant maps are depicted in plane-I_2 with respect to I_3. Notably, the upstream linear boundary of the Lumley triangle is omitted from these Figures due to the experimental constraints, which are confined to the boundaries of axially symmetric contraction and expansion on the right and left sides of the Lumley triangle. Furthermore, the test data at different densities are categorized into three groups: near the bed (in blue, approximately 20% depth); close to the water surface (in red); and the intermediate region (in yellow). Consequently, at a specific longitudinal distance from the start of the 3D pool, the progression of non-isotropic turbulence initiates from the blue dashed lines representing the data and extends towards the water surface as the vertical distance from the flume bed increases. Across various levels of vegetation density (Figures 5–7) and even in the bare channel (Figure 4), most data points are located close to the channel bed and tend to lean towards the left side of the Lumley triangle, remaining near it. However, the disturbances that are not uniform in all directions are mainly found near the bed, close to the border of axially symmetric contraction. As the flow depth increases and the distance from the bed grows, these disturbances transition into a more uniform region before eventually approaching the boundary of axially symmetric expansion. This shift indicates that as the flow depth increases, the tendency for non-uniform turbulence to display three-dimensional characteristics decreases. In the bare channel (Figure 4), the patterns of non-uniform disturbances from the beginning to the end of the 3D pool show that near the bed, these disturbances align with the contraction boundary. As the flow depth increases, the trends move towards the right side of Lumley's triangle, crossing the boundary of plane strain and eventually reaching the expansion boundary. This evolution suggests that the non-uniform disturbances shift from the contraction boundary to the expansion boundary as they move away from the channel bed. In the section where the flow slows down (X/"λ" = 0.21 for all Runs), the data at the bed fall within the region of uniformity.

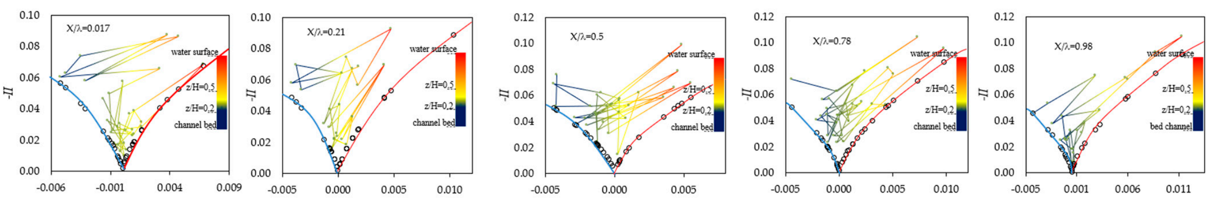

Figure 4. AIMs of Run IV at bare pool.

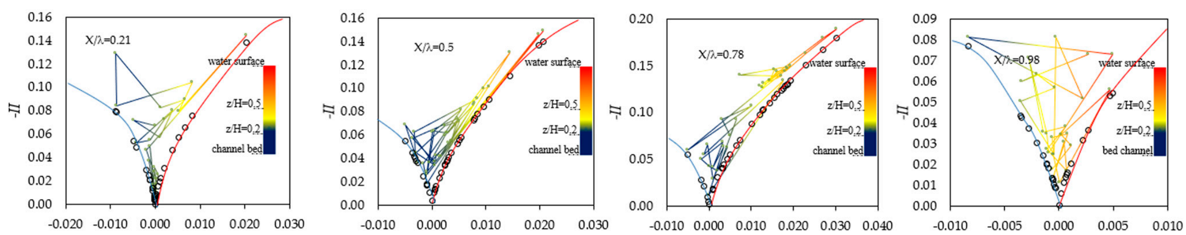

Figure 5. AIMs of Run III.

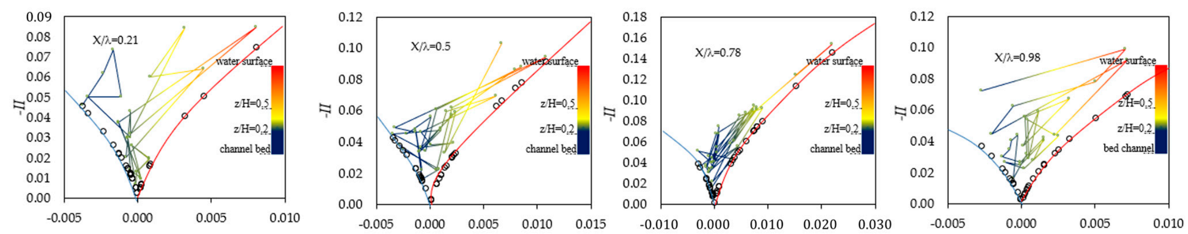

Figure 6. AIMs of Run II.

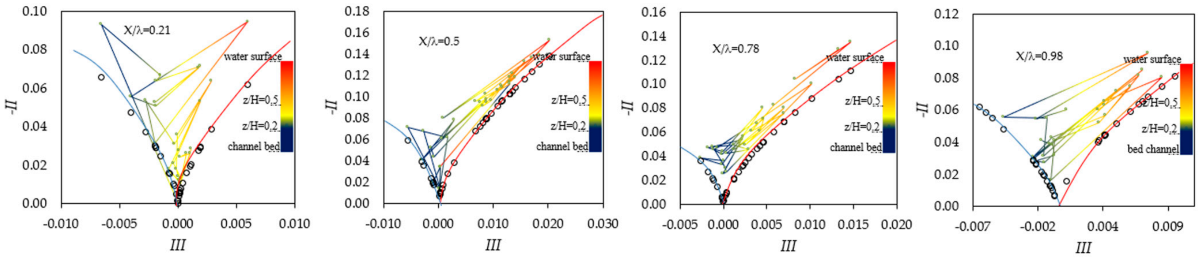

Figure 7. AIMs of Run I.

When vegetation elements are introduced, they show a partial shift towards the right side of Lumley's triangle, indicating that with higher vegetation density (Run 1 in Figure 7), the non-uniform disturbances move towards the expansion limit while still leaning towards uniformity. Within the pool section (X/"λ" = 0.5), and with increased vegetation, the non-uniform turbulence moves away from the contraction boundary, converging completely towards the expansion boundary with denser vegetation. This implies that densely distributed vegetation may reduce the tendency for non-uniform turbulence to become fully three-dimensional. In the section where the flow accelerates (X/"λ" = 0.78 for all Runs), similar to the pool section, the introduction of vegetation causes the non-uniform disturbances to shift from the contraction boundary to the expansion boundary. Particularly near the bed, most data points fall within the region of uniformity of Lumley's triangle, but with higher vegetation density, they move away from the plane strain boundary towards the non-uniform expansion boundary. This behavior suggests a tendency towards the single-component boundary, indicating that the uneven distribution of vegetation elements contributes to increased velocity fluctuations along the flow path, subsequently enhancing the normal stress in the direction of the flow. Towards the downstream part of the pool (X/"λ" = 0.98 for all Runs), turbulence affected by the presence of vegetation initially clusters within the region of uniformity before moving towards the expansion boundary with increasing vegetation density. This indicates that the flow is still influenced by significant disturbances due to the uneven distribution of vegetation elements and pressure gradients in the accelerating and decelerating flow sections, suggesting that the flow has not yet stabilized. Overall, the uneven distribution of rigid vegetation elements in the 3D pool leads to an expanded spherical non-uniform disturbance near the bed and an extended spherical non-uniform disturbance near the water surface. The results suggest that non-uniform turbulence without vegetation tends to align with the plane strain boundary.

It is important to note that Figures 4–7 do not explicitly show how turbulence anisotropy changes with vertical distance at a given streamwise distance. To this end, we introduce the anisotropic invariant function F [10,11]. It is formulated as follows:

$$\mathrm{F} = 1 + 9I_2 + 27I_3. \tag{4}$$

The anisotropic invariant function F provides a perspective on turbulence anisotropy, spanning from the two-component extreme (located at the upper-linear side of the Lumley triangle), represented by F = 0, to the isotropic extreme (situated at the lower vertex of the Lumley triangle), denoted by F = 1 [11]. Thus, it is established that the range of F values lies between 0 and 1. Figure 8a shows the changes in the anisotropic invariant function of the F_0 basis in the upstream pool region, where the flow is uniform. In Figure 8b–e, F_0 is represented by a red dashed line. Figures 9–11 include the corresponding F_0 values from Figure 8 for comparison with varying vegetated densities against the bare channel. Additionally, these figures display the ratio of the height of the vegetated element to flow depth ($\bar{h}_p/H$), which varies along the bedform. The measured ratios in the decelerating flow sections, pool section, accelerating flow section, and downstream section of the pool are 0.26, 0.22, 0.24, and 0.25, respectively, as shown in Figure 9a–d.

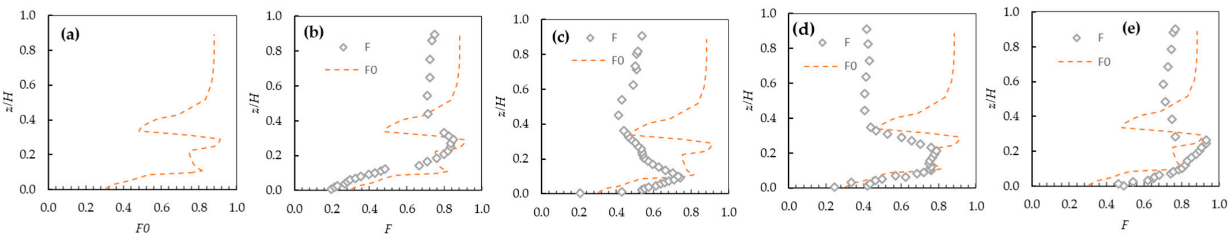

Figure 8. Anisotropic invariant function F versus z/h for Run IV in bare channel: (**a**) bedform upstream; (**b**) pool inlet; (**c**) pool; (**d**) pool outlet; (**e**) bedform downstream.

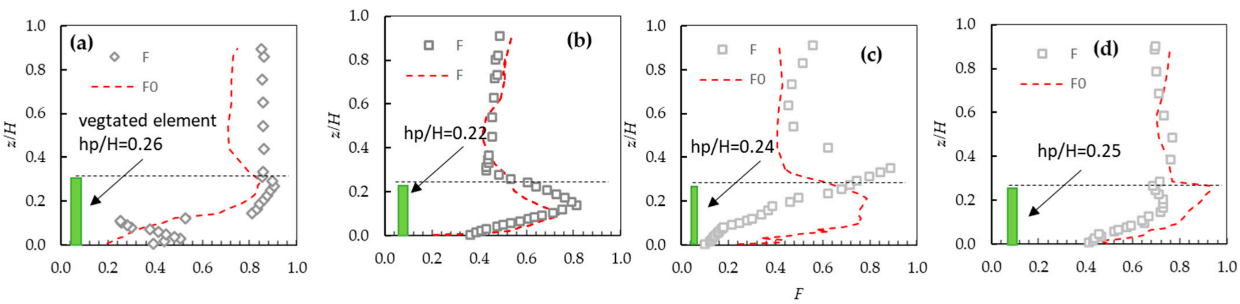

Figure 9. Anisotropic invariant function F versus z/h for Run III: (**a**) pool inlet; (**b**) pool; (**c**) pool outlet; (**d**) bedform downstream.

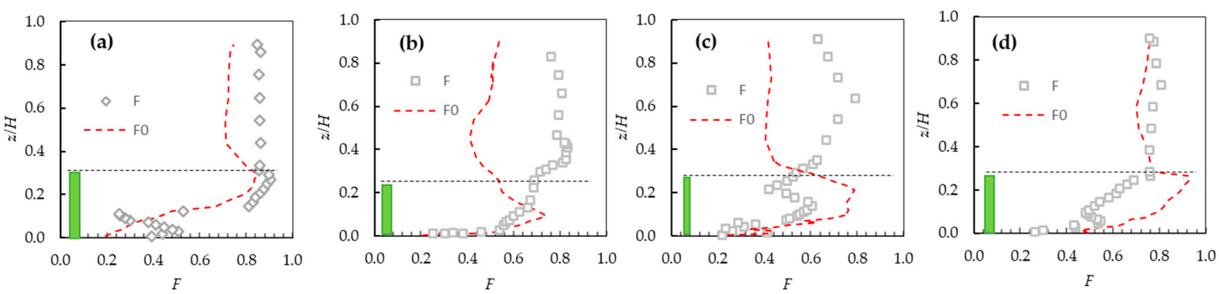

Figure 10. Anisotropic invariant function F versus z/h for Run II: (**a**) pool inlet; (**b**) pool; (**c**) pool outlet; (**d**) bedform downstream.

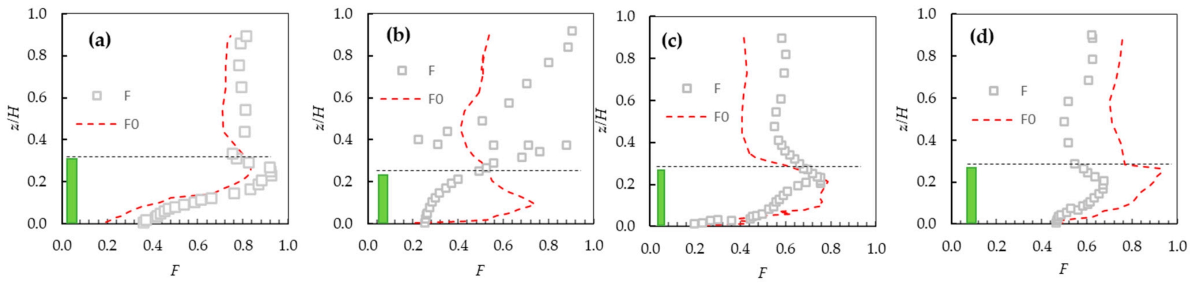

Figure 11. Anisotropic invariant function F versus z/h for Run I: (**a**) pool inlet; (**b**) pool; (**c**) pool outlet; (**d**) bedform downstream.

However, in this research, F values ranged from 0.1 to 0.93 based on the measurement location and vegetation density. Figures 8–11 illustrate variations of the anisotropy invariant function F with respect to the dimensionless vertical distance z/H along the length of the 3D pool, encompassing different flow sections such as the uniform flow section upstream of the pool (Figure 8a) at X/"λ" = 0.017, the decelerating flow section (Figure 8b, a and a) at X/"λ" = 0.21, the mid-section of the pool (Figure 8c, b and b) at X/"λ" = 0.5, the accelerating flow section (Figure 8d, c and c) at X/"λ" = 0.78, and the downstream part of the pool (Figure 8e, d and d) at X/“λ” = 0.98, as well as the bare channel. In the upstream portion of the bare channel depicted in Figure 7 at X/“λ” = 0.017, where the flow is uniform, it appears that the anisotropic turbulence tends towards the isotropic boundary as the flow depth increases up to z/H = 0.3. Beyond z/H = 0.3, as the flow nears the top of vegetated elements, there is a shift towards the two-component boundary before returning to the isotropic boundary with a reverse beak tip movement. In the accelerating flow section near the bed (present in all Figures at X/“λ” = 0.78), the anisotropic turbulence resides at the two-component boundary near the bed and transitions towards the isotropic boundary as the distance from the bed increases.

This suggests that close to the bed, the anisotropy disturbance appears as an elliptical disc, while at greater distances from the bed, spherical anisotropy disturbance prevails, equalizing the main Reynolds stresses in all three directions. In the bare channel at X/“λ” = 0.21 in Figure 8, the F value fluctuates between 0.2 and 0.85. Introducing vegetated elements into the 3D pool and increasing vegetation density (from Run IV in Figure 8 to Run 1 in Figure 11) with an irregular and scattered distribution causes the accompanying anisotropy disturbance to oscillate between the two-component boundary and the isotropic boundary, a fluctuation that continues up to the water surface. In both the decelerating flow section (X/“λ” = 0.21) and the accelerating flow section near the bed (X/“λ” = 0.78), the anisotropic turbulence tends towards the two-component boundary. As the distance from the bed increases up to z/H = 0.2, the F value rises, eventually reaching the water surface by creating an inverted rostral shape between the spherical anisotropy turbulence and the elliptical disc. With the addition of vegetated elements at X/“λ” = 0.78 for all Runs, the maximum F value occurs at a greater distance from the flume bed, with the anisotropy disturbance moving away from the two-component boundary towards the isotropic boundary. However, increasing density shifts the maximum F value closer to the flume bed, indicating a tendency towards isotropy.

The behavior of anisotropic turbulence in the downstream part of the 3D pool (at X/“λ” = 0.98) mirrors that of the normal flow section upstream of the 3D pool at X/“λ” = 0.017 in Figure 7. Near the bed, the anisotropic turbulence is confined to the two-component boundary, transitioning towards isotropy as the distance from the bed increases. The introduction of vegetated elements with a scattered distribution significantly impacts flow characteristics, causing the anisotropic turbulence to oscillate between the two-component boundary and the isotropic boundary in a reciprocating rostral tip pattern. Overall, the flow structure in the presence of vegetation and bed forms exhibits a highly intricate behavior. The irregular distribution of vegetated elements within the 3D pool intensifies this complexity. The presence of a 3D pool with scattered vegetated elements results in a pronounced spherical isotropic disturbance moving away from the bed; approaching the bed, the disturbance takes on a two-dimensional form due to the roughness induced by the vegetated elements.

In the cross-section of the uniform flow in Figure 8a, F_0 ranged from 0.3 to 0.9. When the flow entered the pool in Figure 8c, these values decreased and fluctuated between 0.2 and 0.7. In Figures 9–11, as vegetation was added, F values varied from 0.1 to 0.9, depending on vegetation density and measurement position. Notably, the F values increased with greater vegetation density: 0.73 in Figure 8a; 0.81 in Figure 9b; 0.83 in Figure 10b; and 0.9 in Figure 11.

Assumptions and Limitations

Advancements in flow measurement techniques and canopy interaction analysis have steadily enhanced the precision and effectiveness of laboratory methodologies over time. Nonetheless, this study acknowledges the inherent constraints of laboratory approaches. Several default assumptions underlie the experiments:

- The flow path is assumed to be linear without bends in the horizontal plane.
- The bed’s primary morphology resembles a three-dimensional pool.

- Flow is presumed to be non-uniform and steady, with a constant flow rate throughout the experiment.
- Replicating river conditions in a lab setting does not entail scaling down the phenomenon; instead, efforts are made to mimic comparable conditions found in field studies.
- Coarse-grained sediments are deemed insoluble with consistent properties that remain unchanged over time.
- Sediment transport is considered negligible and thus disregarded.
- While the flow rate is constant during testing, variations in flow depth along the flume occur due to the presence of the pool.
- Submerged rigid vegetated elements are accounted for, including the height and diameter of fixed vegetation elements.
- The vegetation density is utterly non-uniform, and vegetation arrangement follows an irregular pattern.

Overall, these assumptions play a critical role in shaping the experimental set up and interpretation of Reynolds stress anisotropy in flows over 3D pools with submerged rigid vegetation, highlighting the importance of considering their potential effects on research outcomes.

4. Conclusions

Studying natural streams is very complex and requires considerable patience and funds to reach a clear understanding. Almost all rivers and natural streams have a 3D deformable bed and scattered vegetation. Classic methods frequently underestimate essential hydraulic parameters, hindering effective stream restoration management. However, few studies compare these effects against traditional estimations and models.

In the uniform flow cross-section, F_0 ranged from 0.3 to 0.9. Upon entering the pool in a bare channel, these values dropped to between 0.2 and 0.7. With the addition of vegetation, F values fluctuated from 0.1 to 0.9, influenced by vegetation density and measurement position. Notably, F values increased with higher vegetation density, rising from 0.73 in the bare channel to 0.9 at a density of 0.007.

This study found that it alters the 3D flow near the bed, indicating a need for further research and focus on this topic for improved restoration. The findings suggest that real conditions, including 3D bedforms and the presence of vegetation, change the Reynolds stress distribution in the flow depth, leading to different estimations from the classic methods in the literature. More investigation is required in this domain to present a more accurate and affordable estimation of the key hydraulic parameters, such as resistance to flow and determination of transport evaluation. Future work could involve conducting large eddy simulations (LES) for various vegetation densities and comparing the numerical results with the experimental findings of this study.

Author Contributions: Conceptualization, K.N. and H.A.; methodology, A.R.R.; software, K.N.; writing—original draft preparation, K.N., H.A., and M.N.-S.; writing—review and editing, M.N.-S.; supervision, H.A., A.R.R., M.N.-S., and M.K. All authors have read and agreed to the published version of the manuscript.

Funding: This research received no external funding.

Data Availability Statement: The data presented in this study are available on request from the corresponding author.

Conflicts of Interest: The authors declare no conflicts of interest.

References

1. Lamb, M.P.; Brun, F.; Fuller, B.M. Hydrodynamics of steep streams with planar coarse-grained beds: Turbulence, flow resistance, and implications for sediment transport. *Water Resour. Res.* **2017**, *53*, 2240–2263. [CrossRef]
2. Rahimi, H.; Fael, C.M.S.; Taborda, C.S.B.; Yuan, S.; Tang, X.; Singh, P.K.; Fardoost, E.; Santos, C.A.V. Numerical modelling of turbulence kinetic energy in open channel flows with mixed-layer vegetation. *Water* **2023**, *15*, 2544. [CrossRef]

3. de Oliveira, L.E.; Yamasaki, T.N.; Janzen, J.G.; Gualtieri, C. Effects of vegetation density on flow, mass exchange and sediment transport in lateral cavities. *J. Hydrol.* **2024**, *632*, 130910. [CrossRef]
4. Maji, S.; Hanmaiahgari, P.R.; Balachandar, R.; Pu, J.H.; Ricardo, A.M.; Ferreira, R.M. A review on hydrodynamics of free surface flows in emergent vegetated channels. *Water* **2020**, *12*, 1218. [CrossRef]
5. Nosrati, K.; Afzalimehr, H.; Sui, J. Drag coefficient of submerged flexible vegetation patches in gravel bed rivers. *Water* **2022**, *14*, 743. [CrossRef]
6. Nosrati, K.; Afzalimehr, H.; Sui, J. Interaction of Irregular Distribution of Submerged Rigid Vegetation and Flow within a Straight Pool. *Water* **2022**, *14*, 2036. [CrossRef]
7. Afzalimehr, H.; Nosrati, K.; Kazem, M. Resistance to Flow in a Cobble-Gravel Bed River with Irregular Vegetation Patches and Pool-Riffle Bedforms (Run study: Padena Marbor River). *Ferdowsi Civ. Eng.* **2021**, *34*, 35–50.
8. Xu, Y.; Nepf, H. Measured and predicted turbulent kinetic energy in flow through emergent vegetation with real plant morphology. *Water Resour. Res.* **2020**, *56*, e2020WR027892. [CrossRef]
9. Savio, M.; Vettori, D.; Biggs, H.; Zampiron, A.; Cameron, S.M.; Stewart, M.; Soulsby, C.; Nikora, V. Hydraulic resistance of artificial vegetation patches in aligned and staggered configurations. *J. Hydraul. Res.* **2023**, *61*, 220–232. [CrossRef]
10. Barman, J.; Kumar, B. Turbulence in a compound channel with the combination of submerged and emergent vegetation. *Phys. Fluids* **2022**, *34*, 045114. [CrossRef]
11. Dey, S.; Paul, P.; Ali, S.Z.; Padhi, E. Reynolds stress anisotropy in flow over two-dimensional rigid dunes. *Proc. R. Soc. A* **2020**, *476*, 20200638. [CrossRef]
12. Brahimi, M.; Afzalimehr, H. Effect of submerged vegetation density on flow under favorable pressure gradient. *SN Appl. Sci.* **2019**, *1*, 57. [CrossRef]
13. Wang, J.; Liu, J.; Sun, Y.; Li, J.; Cao, Z. Flow resistance of emergent rigid vegetation in steady flow. *J. Hydrol. Hydromech.* **2024**, *72*, 207–222. [CrossRef]
14. Xuan, W.; Yang, C.; Wu, X.; Shao, Y.; Bai, Y. A Numerical Model of the Pollutant Transport in Rivers with Multi-Layer Rigid Vegetation. *Water* **2024**, *16*, 1397. [CrossRef]
15. Lumley, J.L.; Newman, G.R. The Structure of Turbulence in a Sheared Flow. *J. Fluid Mech.* **1977**, *82*, 161–178. [CrossRef]
16. Järvelä, J. Effect of submerged flexible vegetation on flow structure and resistance. *J. Hydrol.* **2005**, *307*, 233–241. [CrossRef]
17. Nikora, N.; Nikora, V.; O'Donoghue, T. Velocity profiles in vegetated open-channel flows: Combined effects of multiple mechanisms. *J. Hydraul. Eng.* **2013**, *139*, 1021–1032. [CrossRef]
18. Devi, T.B.; Kumar, B. Experimentation on submerged flow over flexible vegetation patches with downward seepage. *Ecol. Eng.* **2016**, *91*, 158–168. [CrossRef]
19. Barahimi, M.; Sui, J. Effects of Submerged Vegetation Arrangement Patterns and Density on Flow Structure. *Water* **2023**, *15*, 176. [CrossRef]
20. Sarkar, S.; Dey, S. Turbulence in wall-wake flow downstream of an isolated dune. In *Recent Trends in Environmental Hydraulics: 38th International School of Hydraulics*; Springer: Berlin/Heidelberg, Germany, 2020.
21. Wang, C.; Wang, C. Turbulent characteristics in open-channel flow with emergent and submerged macrophytes. *Adv. Water Sci.* **2010**, *21*, 816–822.
22. Moin, P.; Mahesh, K. Direct numerical simulation: A tool in turbulence research. *Annu. Rev. Fluid Mech.* **1998**, *30*, 539–578. [CrossRef]
23. Nakagawa, H. *Turbulence in Open Channel Flows*; Routledge: London, UK, 2017.
24. Emory, M.; Iaccarino, G. Visualizing turbulence anisotropy in the spatial domain with componentality contours. *Cent. Turbul. Res. Annu. Res. Briefs* **2014**, 123–138.
25. Caroppi, G.; Gualtieri, P.; Fontana, N.; Giugni, M. Vegetated channel flows: Turbulence anisotropy at flow–rigid canopy interface. *Geosciences* **2018**, *8*, 259. [CrossRef]
26. Penna, N.; Coscarella, F.; D'Ippolito, A.; Gaudio, R. Anisotropy in the free stream region of turbulent flows through emergent rigid vegetation on rough beds. *Water* **2020**, *12*, 2464. [CrossRef]
27. Pope, S. Turbulent Flows, Cambridge University Press, Cambridge, UK. *Combust. Flame* **2000**, *125*, 1361–1362.
28. Penna, N.; Coscarella, F.; D'Ippolito, A.; Gaudio, R. Effects of fluvial instability on the bed morphology in vegetated channels. *Environ. Fluid Mech.* **2022**, *22*, 619–644. [CrossRef]
29. Kumar, P.; Ojha, A.; Sharma, A. Reynolds stress anisotropy with higher-order turbulence in flow through rigid emergent vegetation: An experimental study. *J. Hydro-Environ. Res.* **2023**, *51*, 32–47. [CrossRef]
30. Nosrati, K.; Afzalimehr, H.; Sui, J.; Reisifar, H.R. Characteristics of turbulent flow in 3-D pools in the presence of submerged rigid vegetation in channel bed. *J. Hydrodyn.* **2024**, *36*, 158–169. [CrossRef]
31. Schlichting, H.; Gersten, K.; Schlichting, H.; Gersten, K. Fundamentals of boundary-layer theory. In *Boundary-Layer Theory*; Springer: Berlin/Heidelberg, Germany, 2000; pp. 29–49.
32. Poggi, D.; Porporato, A.; Ridolfi, L.; Albertson, J.; Katul, G. The effect of vegetation density on canopy sub-layer turbulence. *Bound. Layer Meteorol.* **2004**, *111*, 565–587. [CrossRef]
33. Wang, Z.; Zhang, H.; He, X.; Jiang, Q.; Xu, W.; Tian, W. Effects of vegetation height and relative submergence for rigid submerged vegetation on flow structure in open channel. *Earth Sci. Res. J.* **2022**, *26*, 39–46. [CrossRef]
34. Richards, K. The morphology of riffle-pool sequences. *Earth Surf. Process.* **1976**, *1*, 71–88. [CrossRef]

35. Thompson, D.M. *Pool–Riffle Sequences. Reference Module in Earth Systems and Environmental Sciences*; Elsevier: Amsterdam, The Netherlands, 2018.
36. Lisle, T.E. Particle size variations between bed load and bed material in natural gravel bed channels. *Water Resour. Res.* **1995**, *31*, 1107–1118. [CrossRef]
37. Lisle, T.E.; Hilton, S. Fine bed material in pools of natural gravel bed channels. *Water Resour. Res.* **1999**, *35*, 1291–1304. [CrossRef]
38. Xu, Y.-X.; Wang, W.-J.; Zhang, S.-B.; Zhao, H.-Q.; Chen, X.-K.; Zhang, H.-P. Features and formulae of sediment incipient motion in vegetated flow environment. *J. Hydrodyn.* **2024**, *36*, 331–339. [CrossRef]
39. Wahl, T.L. Analyzing ADV data using WinADV. In *Building Partnerships*; American Society of Civil Engineers: Reston, VA, USA, 2000; pp. 1–10. [CrossRef]
40. Martin, V.; Fisher, T.; Millar, R.; Quick, M. ADV data analysis for turbulent flows: Low correlation problem. In Proceedings of the Hydraulic Measurements and Experimental Methods, Estes Park, CO, USA, 28 July–1 August 2002; pp. 1–10.